Earth and Planetary Science Letters 311 (2011) 275–286

Contents lists available at SciVerse ScienceDirect

Earth and Planetary Science Letters

journal homepage: www.elsevier.com/locate/epsl

Coupled mechanical and hydrothermal modeling of crustal accretion at intermediate to fast spreading ridges

Sonja Theissen-Krah [a,*], Karthik Iyer [a], Lars H. Rüpke [a], Jason Phipps Morgan [b]

[a] The Future Ocean, Leibniz Institute of Marine Sciences (IFM-GEOMAR), Wischhofstr. 1–3, 24148 Kiel, Germany
[b] EAS Department, Cornell University, Ithaca, NY 14850, USA

ARTICLE INFO

Article history:
Received 7 April 2011
Received in revised form 7 September 2011
Accepted 14 September 2011
Available online xxxx

Editor: Y. Ricard

Keywords:
mid-ocean ridge
gabbro glacier
permeability
ocean crust
finite elements

ABSTRACT

The genesis of oceanic crust at intermediate to fast spreading ridges occurs by the crystallization of mantle melts accumulated in at least one shallow melt lens situated below the ridge axis. Seismic reflection data suggest that the depth of this melt lens is inversely correlated with spreading rate and thereby magma supply. The heat released in it by crystallization and melt injection is removed by a combination of hydrothermal cooling and diffusion. Due to the different time scales of hydrothermal cooling and crustal accretion, numerical models have so far focused on only one of the two processes. Here we present the results from a coupled model that solves simultaneously for crustal accretion and hydrothermal cooling. Our approach resolves both processes within one 2D finite-element model that self-consistently solves for crustal, mantle, and hydrothermal flow. The formation of new oceanic crust is approximated as a gabbro glacier, in which the entire lower crust crystallizes in one shallow melt lens.

We find that the depth of the melt lens and the shape of hot (potentially molten) lower crust are highly dependent on the ridge permeability structure. The predicted depth of the melt lens is primarily controlled by the permeability at the ridge axis, whereas the off-axis permeability determines the width of hot lower crust. A detailed comparison of the modeling results with observed locations of the melt lens at intermediate to fast spreading ridges shows that only a relatively narrow range of crustal permeabilities is consistent with observations. In addition, we find significant deviations between models that resolve or parameterize hydrothermal cooling: the predicted crustal thermal structures show major differences for models that predict the same melt lens location. This illustrates the importance of resolving hydrothermal flow in simulations of crustal accretion.

1. Introduction and tectonic background

New oceanic crust and lithosphere are continuously created along the approximately 60,000 km-long mid-ocean ridge (MOR) system that encircles the globe. The general concept for the formation of the oceanic crust at fast to intermediate spreading ridges is described by the crystallization of mantle melts accumulated in at least one melt lens/'magma chamber' below the ridge axis. The latent heat released during cooling and crystallization is believed to be mainly removed by hydrothermal circulation which thereby accounts for 20–25% of Earth's total heat loss (Lowell et al., 2008). The structure of the oceanic lithosphere and the concept of crustal generation are mainly derived from ophiolite studies, in particular the Oman Ophiolite (Boudier et al., 1996; Cann, 1974; Pallister and Hopson, 1981), and geophysical observations (Carbotte et al., 2000; Detrick et al., 1987; Morgan et al., 1994). In these models, either a depth-distributed or localized magma chamber/melt lens is a key feature to explain the formation of new oceanic lithosphere at fast spreading ridges; it is the place where crystallization takes place and it also provides the heat source that drives the hydrothermal system. Sleep (1975) concluded from thermal calculations that a magma chamber at fast spreading ridges must exist. Early models suggested there would be large magma chambers beneath mid-ocean ridges (e.g. Cann, 1974). However, more recent geophysical surveys (e.g. from the East Pacific Rise (EPR)) revealed only small km-wide molten bodies that overlie a low velocity zone interpreted to be a crystal mush (Detrick, 2000; Harding et al., 1989; Herron et al., 1980). Multichannel seismics (MCS) imaged a nearly continuous melt lens at depths ranging from 1.2 to 2.4 km at EPR between 9° and 13°N (Detrick et al., 1987). Further MCS data showed a magma lens at Juan de Fuca Ridge (Carbotte et al., 2006; Morton et al., 1987; Van Ark et al., 2007), Lau Basin (Collier and Sinha, 1990), NEPR and SEPR (Carbotte et al., 1998, 2000; Purdy et al., 1992) and Southeast Indian Ridge (SEIR) (Baran et al., 2005). Typically, the melt lens extends at most ~2 km in width across the axis, with seismic reflection data also consistent with a lens as narrow as ~1 km in width (Kent et al., 2000). These

* Corresponding author. Tel.: +49 431 6002843; fax: +49 431 6002941.
E-mail addresses: stheissen@ifm-geomar.de (S. Theissen-Krah), kiyer@ifm-geomar.de (K. Iyer), lruepke@ifm-geomar.de (L.H. Rüpke), jp369@cornell.edu (J.P. Morgan).

0012-821X/$ – see front matter © 2011 Elsevier B.V. All rights reserved.
doi:10.1016/j.epsl.2011.09.018

data have been summarized by Phipps Morgan and Chen (1993b) and extended by Baran et al. (2005) to show the relationship between spreading velocity and depth to the melt lens. At the ridge-segment scale, the depth to the melt lens seems to depend inversely on the spreading velocity which implies that the melt lens depth at mid-ocean ridges is controlled by the thermal structure and not by the level of neutral buoyancy as has sometimes been proposed to be characteristic for magma chambers beneath volcanoes (Ryan, 1994). Hooft and Detrick (1993) showed that the level of neutral buoyancy at the EPR lies only 100–400 m below the seafloor and therefore much shallower than the observed depth to the melt lens. Further constraints on the shape and size of the hot axial region at fast spreading ridges are given by seismic tomography (Dunn et al., 2000) which suggests that the width of the partial-melt-containing region does not change much from the subaxial melt lens to the subaxial Moho. Based on this observation, Dunn et al. (2000) proposed steep lateral thermal gradients towards the molten body and nearly horizontal isotherms off-axis.

The depth of crystallization is a key question addressed in two end member conceptual models: the gabbro glacier model and the sheeted sill model. The difference between these models lies in where the crystallization of the lower crust occurs. In the gabbro glacier model (Morgan and Chen, 1993b; Quick and Denlinger, 1993; Sleep, 1975) the lower crust crystallizes in a single shallow melt lens perched at the base of the sheeted dike section, and the solidified material flows downward in a gabbro glacier to build the lower gabbro section of the crust. The sheeted sill model assumes the lower crust to be formed in situ, crystallizing from multiple sills situated at various depth levels. No downward flow of solid material is assumed in this model to build the oceanic crust; instead as the crust is injected at depth it will eventually reside off-axis at the same depth (Kelemen et al., 1997). Combinations of both end member models have also been suggested by Boudier et al. (1996), Chen (2001) and Maclennan et al. (2004).

A second question arises from the assumption of a stable melt lens and its dependence on spreading velocity. A clear ridge-scale relationship is seen between the average depth of the melt lens and spreading rate, but variations in the depth of the melt lens are documented on smaller segment scales (Baker, 2009; Carbotte et al., 1998). These transient effects were recently described by France et al. (2009) who found evidence for a dynamic melt lens from studies in the Oman ophiolite and IODP hole 1256 D. They suggested vertical movement at different time scales ranging from tens to 100,000 yrs as a result of eruption, replenishment or variations in magma supply. In addition, Crawford et al. (1999) inferred from seafloor compliance measurements the existence of a second melt lens at the crust mantle boundary.

A third question is related to the role of hydrothermal circulation in the genesis of oceanic crust. Talwani et al. (1971) suggested as early as 1971 that seawater circulates through the oceanic crust to cool it. This became the conventional explanation for the widely known quantitative discrepancy between observed seafloor heat flow and the prediction of models for the conductive cooling and thickening of oceanic lithosphere with age that fit seafloor depths reasonably accurately, yet which do not fit observed heat flow in regions where they fit seafloor depth well, (cf. Sclater and Francheteau, 1970; Stein and Stein, 1992). The discoveries of hydrothermal vent fields (Corliss et al., 1979) were exciting evidence for high-temperature hydrothermal circulation through the crust. While the existence of hydrothermal circulation is now well-known, its depth extent, the upper temperature limit at which seawater penetrates into the crust, and the crustal permeabilites required for seawater circulation are still being discussed. Gregory and Taylor (1981) concluded from isotopic analyses of the Oman Ophiolite that hydrothermal fluids circulate throughout the crust and locally penetrate the peridotites at temperatures of 400–500 °C. Temperatures up to 600–700 °C were suggested by Nehlig and Juteau (1988) from studies in Oman; Manning et al. (2000) saw evidence for even higher temperatures, above 800 °C near the petrological Moho, from studies in Oman and at Hess Deep, the westernmost limit of the Cocos–Nazca spreading center. McCollom and Shock (1998) used thermodynamic reaction-path modeling to show that fluids can extensively penetrate the lower crust at temperatures above 700 °C and up to 900 °C without altering the mineral composition significantly. Koepke et al. (2005) showed with hydrous partial melting experiments at samples from ophiolites and the EPR that hydrothermal circulation starts already at very high temperatures of about 900–1000 °C. The depth of hydrothermal cooling is also important regarding the two end member models that describe crustal formation. The gabbro glacier model only requires hydrothermal cooling in the upper crust whereas in the sheeted sill model hydrothermal circulation must occur in deeper parts of the crust, otherwise the latent heat of sills would cause remelting and sills at different depths cannot crystallize.

Numerical simulations can help to study the interplay between the crystallization of new oceanic crust and hydrothermal circulation. Such simulations of mid ocean ridge processes need to provide: (1) a viable mechanism to create and spread new material at the ridge axis, and (2) a viable mechanism to remove the heat released by crystallization of new crust.

2. Previous models

Several thermal and mechanical models for crustal generation and hydrothermal cooling at fast spreading ridges have been developed over the past 30 yrs. One of the earliest models was developed by Morton and Sleep (1985). In this thermal model, hydrothermal circulation is simulated as a series of heat sinks near the axis and the latent heat of crystallization is treated as a heat source. The hydrothermal heat flux is constrained by adjusting the number of heat sinks until the depth to the melt lens matches measured data.

The thermal and mechanical model suggested by Phipps Morgan and Chen (1993b) simulates the gabbro glacier model for the accretion of the crust by solving for viscous flow. The effect of hydrothermal circulation on heat transport is parameterized by an increased effective thermal conductivity in the permeable layer by a scaling factor (Nusselt number) that ranged from 1 to 12. The best fit with the observed depth to the melt lens was achieved with a Nusselt number of 8 and a cut-off temperature (temperature above which hydrothermal circulation is assumed not to occur due to permeability closure) of 600 °C.

This gabbro glacier model was extended to include a second Moho-level melt lens (Chen, 2001) after seismic observations indicated that there is likely to be additional melt present at the subaxial crust-Moho region. This model suggested that only 0–10% of the gabbros can be emplaced in a second basal melt lens — otherwise the latent heat associated with this deep crustal injection would lead to a large molten body in the lower crust.

A recent model by Machetel and Garrido (2009) describes the response of the temperature field to the distribution of sills and melt lens and different styles of hydrothermal cooling, again parameterized by use of a simple Nusselt number scaling to approximate the heat transport by hydrothermal convection.

In contrast to the models mentioned above that focus primarily on the heat transport associated with the 'supply' side of crustal formation, the numerical model described by Cherkaoui et al. (2003) focuses on solving hydrothermal circulation while new lithosphere accretes continuously and is advected horizontally with spreading velocity. They found that both the gabbro glacier model and the sheeted sill model are likely to be thermally feasible.

A model focusing on the distribution of crystallization developed by Maclennan et al. (2004) indicates that a hybrid model, in which 25–75% of the lower crust forms in a shallow melt lens and the remaining portion crystallize in sills, is able to match the thermal

structure of fast spreading ridges. In this model, the new crust is advected horizontally with the spreading velocity and hydrothermal cooling and latent heat of crystallization is implemented with source terms similar to the approach of Morton and Sleep (1985). Comparing the above mentioned models, it becomes obvious that, regardless of whether the models simulate the gabbro glacier or sheeted sill scenario, previous models have focused either on resolving hydrothermal circulation accurately (e.g. Cherkaoui et al., 2003) or on solving for the mechanics of crustal accretion while parameterizing hydrothermal cooling as an enhanced thermal conductivity or by use of heat sources and sinks (Chen, 2001; Machetel and Garrido, 2009; Maclennan et al., 2004; Morgan and Chen, 1993b). The question if the depth to the melt lens only depends on the spreading rate remained unresolved, as it depends on both the accretion of crust at a source as well as on hydrothermal cooling.

In this study we present a new numerical model which solves explicitly for both processes, the motion of viscous material accreting as a gabbro glacier coupled to a full 2D model of hydrothermal fluid flow. We first reproduce the mechanical model with parameterized hydrothermal cooling of (Morgan and Chen, 1993b) and then implement a more complete treatment for hydrothermal fluid flow by solving the Darcy equations (coupled model). This allows us to explore the differences between the parameterized and the coupled model for the same model configurations. With the coupled model we can also study the influence of subaxial permeability and spreading velocity on the subaxial depth of the melt lens. We will show that the solution is very sensitive to the permeability structure and the applied cut-off temperature for hydrothermal circulation. The depth of the melt lens and the off-axis and vent temperatures will then be compared to predictions of other models and with observed data.

3. Method

Coupling mechanical and hydrothermal numerical models remains challenging due to the different spatial and temporal scales of these processes. The different timescales of magmatic, tectonic and hydrothermal events are summarized in Lowell et al. (1995). The activity of individual hydrothermal vents is estimated to be between 10 and 100 yrs whereas that of a vent field is between 10^3 and 10^6 yrs. In contrast, seafloor spreading at a fast spreading ridge where the crust moves at half rates of 50 km/Myr, so that 5 km of lower crustal flow away from the ridge axis occur on a timescale of ~10^5 yrs. Models of hydrothermal processes tend to use a model time step of less than a year and are typically limited in size to a crustal thickness-scale (Coumou et al., 2006) while numerical experiments describing the process of crustal accretion and subaxial mantle flow (Morgan and Chen, 1993b) need to model thermal evolution over timescales of several million years. Our model aims to simultaneous resolve the development of hydrothermal convection cells while solving for crustal and mantle flow associated with seafloor spreading.

3.1. Governing equations for crustal accretion

Viscous flow in the crust and mantle can be described by the strong from of plane strain Stokes flow:

$$\mathrm{x-direction}: \frac{\partial}{\partial x}\left(\mu\left(\frac{4}{3}\frac{\partial u_x^m}{\partial x}-\frac{2}{3}\frac{\partial u_y^m}{\partial y}\right)\right)+\frac{\partial}{\partial y}\left(\mu\left(\frac{\partial u_x^m}{\partial y}+\frac{\partial u_y^m}{\partial x}\right)\right)-\frac{\partial P}{\partial x}=0 \quad (1)$$

$$\mathrm{y-direction}: \frac{\partial}{\partial y}\left(\mu\left(-\frac{2}{3}\frac{\partial u_x^m}{\partial x}+\frac{4}{3}\frac{\partial u_y^m}{\partial y}\right)\right)+\frac{\partial}{\partial x}\left(\mu\left(\frac{\partial u_x^m}{\partial y}+\frac{\partial u_y^m}{\partial x}\right)\right)-\frac{\partial P}{\partial y}+\rho g_y=0 \quad (2)$$

$$\mathit{Pressure}: \nabla\cdot\vec{u}_m+\frac{P}{\lambda^p}=0 \quad (3)$$

where u_m, μ, ρ, g and P are viscous (solid) velocities, viscosity, density, vertical component of gravity and pressure, respectively. Bulk viscosity is zero in Stokes flow and λ^p is a large penalty factor to achieve incompressibility and zero bulk deformation. All symbols and variables used in this study are listed in Table 1.

We assume incompressibility except in the regions of dike injection and the melt lens where magma is injected via a dilation term $\dot{\psi}$ following the approach of Phipps Morgan and Chen (1993b). Eq. (3) is therefore modified to:

$$\nabla\cdot\vec{u}_m+\frac{P}{\lambda^p}=\dot{\psi}. \quad (4)$$

In the gabbro glacier model all the lower crust crystallizes in the melt lens and all the upper crust in the diking region. The injection rates ($\dot{\psi}$) for the lower crust and the upper crust (intrusives) are:

$$\dot{\psi}_{lc}=\frac{v_s h_{lc}}{h_{ml}w_{ml}}$$
$$\dot{\psi}_{dikes}=\frac{v_s h_{dikes}}{h_{dikes}w_{dikes}}=\frac{v_s}{w_{dikes}} \quad (5)$$

with v_s, h and w being spreading rate, thickness and width of dikes (*dikes*), melt lens (*ml*) and lower crust (*lc*), respectively. The dilation term is constant in the dikes while it changes in the melt lens, since

Table 1
List of variables.

Symbol	Variable	Value	Unit
P	Pressure		Pa
T	Temperature		°C
g	Gravitational acceleration	9.81	m/s^2
v_s	Full spreading rate	50–150	mm/yr
$\dot{\psi}$	Dilation term/magma injection		1/s
H_f	Latent heat of crystallization	1.1×10^9	J/m^3
L	Total heat released		J/m^3
Matrix properties			
k^0_{axis}	Surface permeability at ridge axis	2×10^{-15}–6×10^{-15}	m^2
$k^0_{off\text{-}axis}$	Surface permeability off-axis	2×10^{-15} or 10^{-16}	m^2
c	Decay constant for permeability	8×10^{-4} or 3×10^{-4}	m^{-1}
u_m	Viscous velocity		m/s
λ_c	Thermal conductivity crust	3.3	W/m^2 K
λ_m	Thermal conductivity mantle	3.3	W/m^2 K
ρ_m	Density mantle	3300	kg/m^3
ρ_c	Denstity crust	3300	kg/m^3
ϕ	Porosity	0.01	
c_{pm}	Specific heat capacity	1000	J/kg K
μ	Viscosity:		
	Asthenosphere	10^{19}	Pa s
	Lithosphere	10^{23}	
	Crust above 750 °C	10^{16}	
λ^p	Penalty factor	10^4	
Fluid properties			
q	Darcy velocity		m/s
ρ_f	Density	Tables	kg/m^3
u_f	Pore velocity		m/s
c_{pf}	Specific heat capacity	Tables	J/kg K
μ_f	Viscosity	Tables	Pa s

the size of the melt lens is kept constant whereas the height of the dikes depends on the depth to the melt lens.

Our formulation does not resolve the various processes that bring the melt to the melt lens but simply accounts for them by a source dilation term in the melt lens and diking region (Eq. (5)). Notice also that the contraction term that should account for the extraction of melt from the asthenosphere is neglected because it only has a minor effect on mantle flow for normal crustal thicknesses (Cordery and Morgan, 1992; Schmeling and Marquart, 2008). The effect of the dilation term can be seen in Fig. 2, which only shows outflow as a consequence of melt injection via the dilation term.

3.2. Parameterized hydrothermal cooling

Cooling by hydrothermal convection is often parameterized in terms of an effective thermal conductivity. The non-dimensional Nusselt number describes the relative efficiency of convective (hydrothermal) cooling with respect to heat loss by conduction. Within a purely conductive model, the convective heat loss can therefore be approximated by using a thermal conductivity that is enhanced by the assumed Nusselt number of the system. With these assumptions, the heat equation can be written as:

$$\rho_m c_{pm} \frac{\partial T}{\partial t} = -\rho_m c_{pm} \vec{u}_m \cdot \nabla T + \nabla \cdot Nu \lambda \nabla T + L\dot{\psi} \tag{6}$$

where ρ_m, c_{pm} and $\vec{u}_m$ are density, specific heat and the velocity of the matrix, respectively. The thermal conductivity (λ) is multiplied with the non-dimensional Nusselt number. The source term L consists of the latent heat released during crystallization of the melt lens (H_f) and heating by melt injection:

$$L = H_f + \left(T_{liq} - T\right)\rho_m c_{pm}. \tag{7}$$

As stated above, the gabbro glacier assumption used here does not make predictions on the rates and patterns of crystallization. Melt is instantaneously added to the melt lens, where the entire lower crust crystallizes. The entire upper crust crystallizes in the diking region.

3.3. Resolved hydrothermal circulation

Resolving hydrothermal cooling instead of parameterizing it requires solving for Darcy-type fluid flow. In a deformable matrix, single (fluid) phase Darcy-flow can be written as:

$$\vec{q} = \phi\left(\vec{u}_f - \vec{u}_m\right) = -\frac{k}{\mu_f}\left(\nabla P_f - \rho_f \vec{g}\right) \tag{8}$$

where $\vec{q}$ is the Darcy velocity, ϕ is porosity, k is permeability, $\vec{u}_f$ is pore velocity, $\vec{u}_m$ is velocity of the matrix, μ_f, ρ_f and P_f are viscosity and density of the fluid and fluid pressure, respectively. The single phase assumption is warranted since we restrict our simulations to pure water convection and to pressure regimes beyond the critical end-point.

Eq. (9) describes the full solid and fluid mass conservation:

$$\frac{\partial \phi \rho_f}{\partial t} + \frac{\partial (1-\phi)\rho_m}{\partial t} = -\nabla \cdot \left(\phi \rho_f \vec{u}_f\right) - \nabla \cdot \left((1-\phi)\rho_m \vec{u}_m\right). \tag{9}$$

Since we assume incompressible solid flow and constant porosity, the second terms on the right- and left-hand sides vanish. A fluid pressure equation for a compressible pore fluid inside an incompressible matrix can be derived by substituting Eq. (8) into Eq. (9) and by realizing that the term $\nabla \cdot \left(\phi \rho_f \vec{u}_m\right)$ reduces to $\vec{u}_m \phi \nabla \rho_f$, which can be neglected for the largely horizontal solid flows considered in this study:

$$\nabla \cdot \left[\frac{k\rho_f}{\mu_f}\left(\nabla P_f - \rho_f \vec{g}\right)\right] = \phi \frac{\partial \rho_f}{\partial t} \approx 0. \tag{10}$$

For simplification (and better numerical performance) the term $\phi \frac{\partial \rho_f}{\partial t}$ is neglected based on the argument that the characteristic fluid pressure diffusion time scales ($^k/_{\phi \beta \mu_f}$), with β = compressibility, in the simulations are short (years to tens of years) compared to the system time scales. This approach is similar to the simulations of Fehn and Cathles (1979).

The permeability in the coupled model decays exponentially with depth and changes by about two orders of magnitude throughout the crust.

$$k_i(y) = k_i^0 \exp(c_i y) \tag{11}$$

where k_i and $k^0{}_i$ are permeability and permeability at the surface (seafloor) respectively and c_i ($c = 8 \times 10^{-4}\,\mathrm{m}^{-1}$) is the decay constant. The index i refers to on- or off-axis permeabilities. The permeabilities described for the different simulations all refer to the surface (seafloor) permeability k^0. The porosity is assumed to be constant in our models, although porosity probably changes due to compaction and alteration processes. Porosity and permeability are linked but not necessarily directly related. The permeability might not always be derived from the total amount of porosity. More important are shape and connectivity of single pores (Violay et al., 2010) and we consider the permeability to be independent from porosity.

The full energy balance for hydrothermal flow in local thermal equilibrium in terms of internal energy is, for example, given by Faust and Mercer (1979). Here we follow Bird et al. (2007) and use an energy balance equation in terms of temperature, which is composed of solid and fluid advection, thermal diffusion, and latent heat of crystallization and melt injection as source terms (L):

$$\begin{aligned}(1-\phi)\rho_m c_{pm} \frac{\partial T}{\partial t} + \phi \rho_f c_{pf} \frac{\partial T}{\partial t} \\ = -(1-\phi)\rho_m c_{pm} \vec{u}_m \cdot \nabla T - \phi \rho_f c_{pf} \vec{u}_f \nabla \cdot T + \nabla \cdot (\lambda \nabla T) + L\dot{\psi}.\end{aligned} \tag{12}$$

The indices f and m denote fluid and matrix properties, respectively. Following the rationale of Garg and Pritchett (1977), pressure volume work and viscous dissipation are neglected in the energy balance for the here considered pressure and temperature ranges of crustal scale supercritical hydrothermal flow. Substituting Darcy velocities $\vec{q} = \phi\left(\vec{u}_f - \vec{u}_m\right)$ leads to:

$$\left(\rho c_p\right)_{bulk} \frac{\partial T}{\partial t} = -\left(\rho c_p\right)_{bulk} \vec{u}_m \cdot \nabla T - \rho_f c_{pf} \vec{q} \cdot \nabla T + \nabla \cdot (\lambda \nabla T) + L\dot{\psi} \tag{13}$$

where $(\rho c_p)_{bulk} = \phi \rho_f c_{pf} + (1-\phi)\rho_m c_{pm}$.

Note that the main difference to the parameterized heat equation is the changed $(\rho c_p)_{bulk}$ term and the heat advection by porous convection. The fluid properties (density, viscosity and specific heat capacity) are functions of pressure and temperature and are acquired from pre-calculated look-up tables computed with the PROST (PROperties of water and Steam, http://www.enersim.de/download/PROST4.html (Bauer, 1998)) program. This program uses the IAPS-84 formulation to compute the properties of water and steam.

The coupling between hydrothermal flow and the mechanics of crustal accretion is restricted here to temperature and its feedbacks into viscosity and density. Future models will hopefully be able to couple hydrothermal and solid flow more rigorously. For example, in the here presented formulation, fluid and solid pressures/stresses are computed independently of each other.

3.4. Model setup and implementation

We consider an idealized mid-ocean ridge where half of the domain is modeled assuming symmetric spreading at the ridge axis. The depth to the melt lens is controlled by the 1200 °C isotherm, which may change during every time step until a steady-state is reached. The ridge axis in the model is at the left boundary (Fig. 1). The two dimensional domains are 60 km wide and 40 km deep with the Moho at 6 km. The lower crust is generated in a 200 m thick and 1 km wide melt lens as assumed in the gabbro glacier model (the dimensions are described for half of the domain). The crustal accretion of rocks below the magma solidus (dike injection and lava and pillow flows) occurs in a 200 m wide diking region at the ridge axis which extends to the top of the melt lens. The temperatures at the bottom is fixed to 1350 °C and the pressure at the top is assumed to be 250 bars for a seafloor depth of ~2.5 km. Fluids that enter the box are fixed to 2 °C and can leave the system through the top boundary with computed temperatures. The initial temperature is linear in the crust and constant in the mantle. The analytical solution for isoviscous passive mantle flow (cf. Chen and Morgan, 1990) is applied to the bottom and mantle right hand boundary in both models (parameterized mechanical and coupled models). The boundary between asthenosphere and lithosphere in the mantle is determined by the 750 °C isotherm. The modeled viscosity contrast is about 10^4 Pa s from 10^{19} (asthenosphere) to 10^{23} (lithosphere) at this boundary. A second viscosity contrast is applied in the crust and is also defined by the 750 °C isotherm. The viscosity in the hot crust is 10^3 lower than in the asthenosphere (10^{16} Pa s). The viscosity in the dikes decreases by an order of magnitude in comparison to the cold lithosphere. The Moho acts as an internal boundary, i.e. no flow is allowed across the Moho. Hydrothermal cooling is assumed to occur in the crust up to a cracking temperature of 600 °C. In the coupled model, we assume a region of higher permeability situated at the ridge axis (1 km wide) to focus venting (cf. Coumou et al., 2009). The crust away from the ridge axis has lower permeabilites to account for processes that may decrease permeability (e.g. mineral precipitation). The permeability is depth dependent (cf. Section 3.3) in both regions (on- and off-axis). The mantle, melt lens and the region below the melt lens are impermeable.

The equations for Stokes flow, Darcy flow and thermal diffusion are solved with a 2D finite element method implemented into a modified version of the MATLAB code MILAMIN (Dabrowski et al., 2008). The mechanics part (Stokes flow) is solved on a 7 node triangular mesh with quadratic velocity shape functions and discontinuous linear pressure variations. The pressure in Eq. (4) is solved with a penalty-type method implemented in an iterative Uzawa-like form, see Dabrowski et al. (2008) or Zienkiewicz and Taylor (2000) for details.

The Darcy pressure and velocities are calculated on 6 node triangles with quadratic pressure variations and linear velocities. The diffusion equation is solved using a fully implicit scheme. Advection is resolved with a semi-Lagrangian scheme. The mesh density is highest in the near-axis region and the upper crust, where the porous solver requires higher resolution due to relatively high flow rates. The near-axis resolution is about 30 m while the resolution in the upper crust off-axis is about 100 m. The model calculates the depth to the 1200 °C isotherm (defines the top of the melt lens) at the ridge axis at every time step and the top of the melt lens is set to this depth. The temperatures at the left hand boundary are interpolated to move the melt lens with 10 m accuracy. This leads to a new model geometry, remeshing and an update of the matrix properties and viscous velocities. The modeling algorithm first calculates the viscous velocities and fluid properties and then iteratively solves for (1) hydrothermal circulation in the crust including the calculation of fluid pressure, fluid velocities and fluid advection, (2) solid advection, (3) new depth of the melt lens and remeshing, (4) update of solid velocities and fluid properties and (5) thermal diffusion. All numerical models were run for at least 1 Myr, where each time step is limited by the porous flow solver, which is a few years or less, depending on permeability. All simulations conducted with the coupled model are listed in Table 2.

4. Results

4.1. Nusselt number parameterization

The first set of simulations is performed with the Nusselt number parameterization, i.e. with an eight-fold increased conductivity in the crust where temperatures are below 600 °C ($T_{cut\text{-}off} = 600$ °C), for different spreading rates. The modeling time is 2 Ma although a steady state melt lens is reached after about 30,000 yrs. Fig. 2 shows the temperature structure and solid flow field after 1 Ma for a full spreading rate of 110 mm/yr. This time, 1 Ma, corresponds roughly to the time for the lithosphere to reach thermal equilibrium up to a few 10 kms away from the ridge which is the width of our computation box. The depth to the melt lens reaches a steady state and is plotted against spreading velocity in Fig. 3. All the heat is removed for lower spreading rates (less than 60 mm/yr) so that no stable melt lens can exist in the subaxial crust. All experiments either reach a steady state or the system is cooled completely and the melt lens (1200 °C isotherm) lies below the Moho at the ridge axis. The depth to the melt lens is, as expected, inversely correlated to spreading rate. Temperatures are generally higher at faster spreading velocities, however there is no linear relation between spreading rate and depth to the melt lens. Fig. 3 shows two different trends: for very fast to intermediate spreading velocities (150–80 mm/yr) the depth to the melt lens increases slowly with decreasing spreading rate (about 1 km). At slow intermediate rates, the depth to the melt lens changes more rapidly with spreading velocity; for example, variations of about 1.5 km for a range of spreading velocities of 20 mm/yr (80–60 mm/yr) can be seen in Fig. 3. The results are similar to the numerical experiments

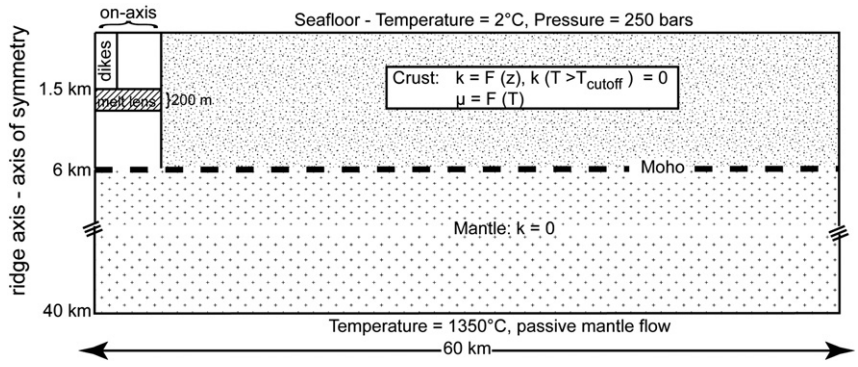

Fig. 1. Model setup.

Table 2
List of simulations.

Full spreading rate (mm/yr)	Surface permeability k^0 on-axis (m^2)	Depth to the melt lens (km)	Additional changes
Permeability changes by two orders of magnitude ($c = 8\times10^{-4}\ m^{-1}$), cut-off = 600 °C, permeability off-axis = $1\times10^{-16}\ m^2$			
40	4×10^{-15}	No melt lens	
50	4×10^{-15}	3.0	
50	6×10^{-15}	No melt lens	
60	4×10^{-15}	2.6	
60	6×10^{-15}	3.3	
70	3×10^{-15}	1.7	
70	4×10^{-15}	2.3	
70	6×10^{-15}	2.9	
80	3×10^{-15}	1.9	
80	4×10^{-15}	2.0	
80	6×10^{-15}	2.6	
110	2×10^{-15}	0.5	
110	3×10^{-15}	1.0	
110	4×10^{-15}	1.1	
110	6×10^{-15}	1.6	
110	1×10^{-14}	2.8	
110	3×10^{-14}	4.8	
110	5×10^{-14}	No melt lens	
150	3×10^{-15}	0.5	
150	4×10^{-15}	0.7	
150	6×10^{-15}	1.1	
Cut-off temperature = 700 °C			
70	3×10^{-15}	4.1	
80	3×10^{-15}	3.2	
150	3×10^{-15}	0.6	
Permeability changes **one order** *of magnitude throughout the crust ($c = 3\times10^{-4}\ m^{-1}$)*			
50	3×10^{-15}	No melt lens	
60	3×10^{-15}	3.8	
70	3×10^{-15}	3.1	
110	3×10^{-15}	1.1	
110	3×10^{-15}	1.6	Cut-off T = 700
110	4×10^{-15}	1.8	
110	4×10^{-15}	2.3	Crustal thickness = 5 km
110	4×10^{-15}	0.8	Crustal thickness = 10 km
110	6×10^{-15}	3.1	
Surface permeability off-axis $k^0 = 2\times10^{-15}\ m^2$			
110	4×10^{-15}	1.0	

documented in Phipps Morgan and Chen (1993b) (red line). Only the computed depth to the melt lens at intermediate spreading rates (60–80 mm/yr) shows an observable difference.

4.2. Coupled model

The second set of numerical experiments was done with the coupled model in which viscous crustal flow and porous hydrothermal flow were solved simultaneously. Near-axis (the region up to 1 km away from the ridge axis) and off-axis surface permeabilities (k^0) were assumed to be $4\times10^{-15}\ m^2$ and $10^{-16}\ m^2$, respectively, for different full spreading rates (50 mm/yr, 60 mm/yr, 70 mm/yr, 80 mm/yr, 110 mm/yr and 150 mm/yr). The temperature structures for different time intervals for a spreading rate of 110 mm/yr are shown in Fig. 4. Note that the final steady-state is independent of the assumed starting conditions (i.e. linear or half-space cooling temperatures) and that the transient results are only shown to exemplify how a steady state is approached. In these numerical experiments, a single convection cell forms at the ridge axis after about 200 yrs and the high temperature upflow at the ridge axis is present throughout the numerical experiments. Hydrothermal cells develop at the ridge axis and above the melt lens and start to migrate towards the right hand side of the modeling domain — similar to kinematic simulations of hydrothermalism at ocean spreading centers (Iyer et al., 2010). The solutions reach a quasi-steady-state after about 50,000–100,000 yrs (Fig. 4) with a stable temperature distribution at the ridge axis (stable melt lens) and hydrothermal plumes migrating away from the ridge axis. The final temperature structure is comparable with the temperatures derived from the plate cooling solution for given spreading rates (Fig. 4). Fig. 5 shows the depth to the melt lens depending on permeability for a spreading velocity corresponding to the EPR at 9°N (110 mm/yr). A melt lens stabilizes in the crust for surface permeabilities lower than $k^0 = 3\times10^{-14}\ m^2$. For higher permeabilities all heat is removed so that no stable melt lens can exist above 6 km.

The convection cell at the ridge axis reaches surface temperatures of about 380–400 °C which are relatively insensitive to spreading velocity or assumed surface permeability. The convection cells developed off-axis in the crust reach much lower venting temperatures of less than 200 °C, typically around 100 °C. This appears to be consistent with the observations at fast spreading ridges where hydrothermal fields are concentrated near the neovolcanic zone and often accompanied by low temperature diffuse discharge off-axis (Baker and German, 2004). The style of hydrothermal convection is also controlled by the depth to the melt lens and therefore by the dimensions

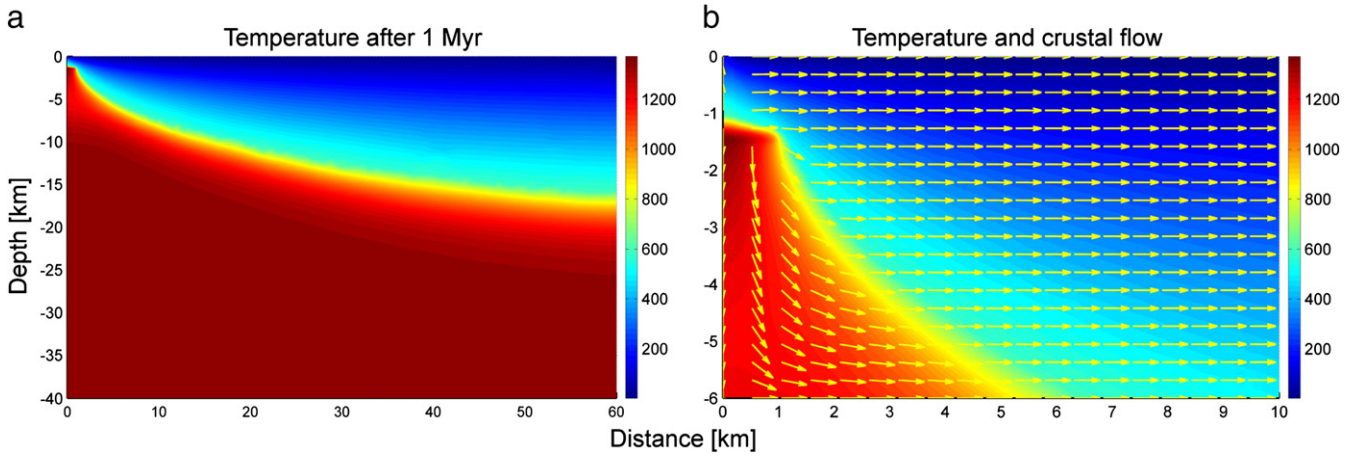

Fig. 2. (a): Temperature after 1 Myr with Nusselt parameterization for a model with 110 mm/yr spreading velocity (comparable to EPR) and an eight fold increase in thermal conductivity in the crust and below a cracking temperature of 600 °C. (b) Shows a more detailed plot of the first 10 km in the crust at the ridge axis. Yellow arrows indicate the crustal flow as a gabbro glacier where the lower crust crystallizes in the shallow melt lens. (For interpretation of the references to color in this figure legend, the reader is referred to the web version of this article.)

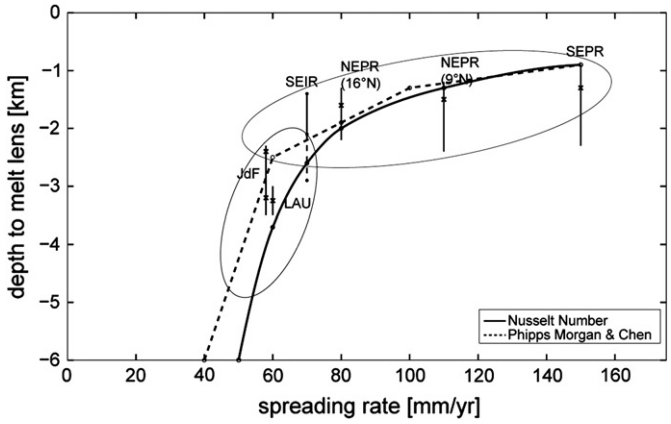

Fig. 3. Depth to the top of the melt lens as function of spreading rate for the Nusselt number parameterization. Dashed line shows the results from Phipps Morgan and Chen (1993a, 1993b) and solid black line are the new modeling results. NEPR = North East Pacific Rise (Carbotte et al., 1998; Detrick et al., 1987), SEPR = Southeast Pacific Rise (Purdy et al., 1992), SEIR = Southeast Indian Ridge (Baran et al., 2005; Carbotte et al., 1998), LAU = Lau basin (Collier and Sinha, 1990), JdF = Juan de Fuca ridge (Carbotte et al., 2006; Morton et al., 1987; Van Ark et al., 2007). Ellipses show transition between axial highs (top right) and rifted axial highs, respectively (bottom left) (e.g. Baran et al., 2005). The observed melt lens at SEIR at 2.9 km (dashed line) coincides with thinner crust.

of the high permeable region above the melt lens. The width is fixed to 1 km (width of the high permeability region above the melt lens) but the depth to the melt lens deepens with higher permeabilites. Two cells develop in a region of 1 km × 1 km to cool the crust for permeabilties lower than 6×10^{-15} m^2 (Fig. 6). An increase in permeability at the ridge axis leads to higher convection speeds and fluids circulate deeper in the crust so that the permeable region can reach down to the Moho for very high permeabilities ($>6\times10^{-15}$ m^2). In these simulations the crust is cooled by one convection cell which is elongated compared to the cells for lower permeabilities. Convection cells seem to form at typical aspect ratios (Coumou et al., 2006) and the number therefore depends on the dimension of the high permeable region above the melt lens which is constrained by permeability (depth to the melt lens) and the width of the melt lens (1 km). The different solutions for hydrothermal convection using different permeabilities in the region above the melt lens are comparable to the simulation of Cherkaoui et al. (2003) who also reported different styles of convection depending on the dimension of the permeable region.

5. Discussion

5.1. Comparison of results using parameterized-hydrothermal and coupled-hydrothermal models

The depth to the melt lens can be fitted well with the parameterized model with a Nusselt number of 8 and the coupled model. The parameterized model and simulations with a surface permeability of 4×10^{-15} m^2 lead to comparable results.

The two main differences between both models are (1) variations in the off-axis temperature structure of the upper crust, (2) the predicted width of the region of hot lower crust, and (3) the formation

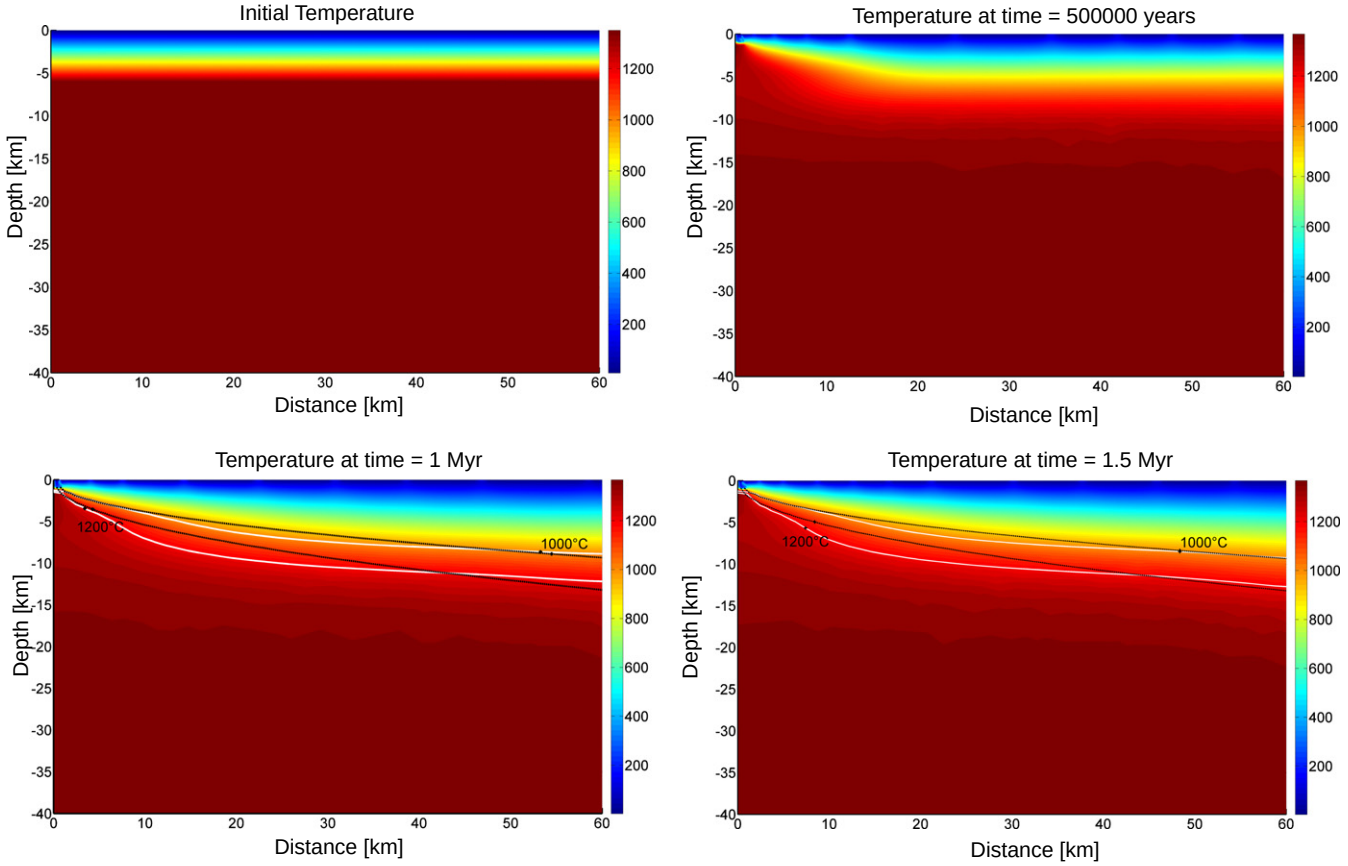

Fig. 4. Temperature evolution for different time steps with coupled model. Quasi-stable convection cells start to develop after 200–600 yrs. The 1000 °C and 1200 °C isotherms are shown for the modeling results (white lines) and the analytical plate cooling solution (black lines).

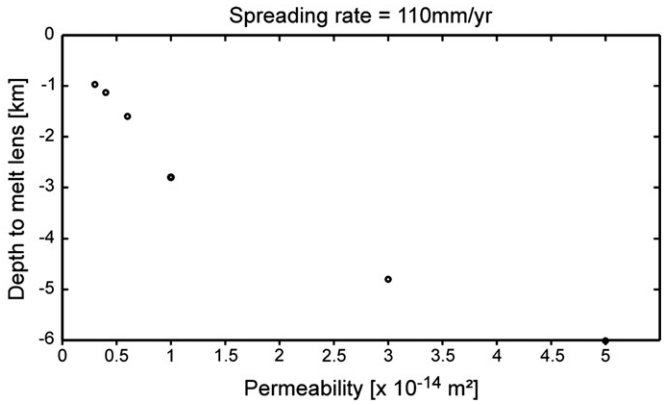

Fig. 5. Depth to the melt lens for different permeabilities for spreading rate of 110 mm/yr. Permeabilities between 3×10^{-15} m^2 and 3×10^{-14} m^2 result in a stable melt lens in the crust. No stable melt lens exists in the crust for higher permeabilities.

of a thermal boundary layer at the base of the hydrothermal flow zone. Conductive cooling in the parameterized model leads to a uniform heat extraction in the entire crust which results in Moho-temperatures of about 300 °C at around 40 km away from the ridge (Fig. 2). In the coupled model, the development of hydrothermal convection cells leads to a more complex temperature structure with venting at the ridge axis and diffuse discharge off-axis (cf. Section 5.2 and Fig. 8).

The width of the hot region of lower crust (1200 °C) differs between both models, i.e. for spreading velocities of 110 mm/yr, the half-width of about 8 km at the base of the crust in the coupled model compared to 1.5–2 km for the parameterized treatment. The width of the hot region broadens by only a few hundred meters for the Nusselt number model through the whole crust. The main difference between both models is seen in the cooling of the off-axis crustal region. The temperature structure off-axis and the width of the hot crust are controlled by the off-axis permeability structure (cf. Section 5.2 and Fig. 8).

5.2. Comparison with observations

5.2.1. Depth to the melt lens

We used the depth to the melt lens as a key benchmark for these experimental results. The depth to the melt lens as a function of spreading velocity for near-axis surface permeabilities of 4×10^{-15} m^2 (red

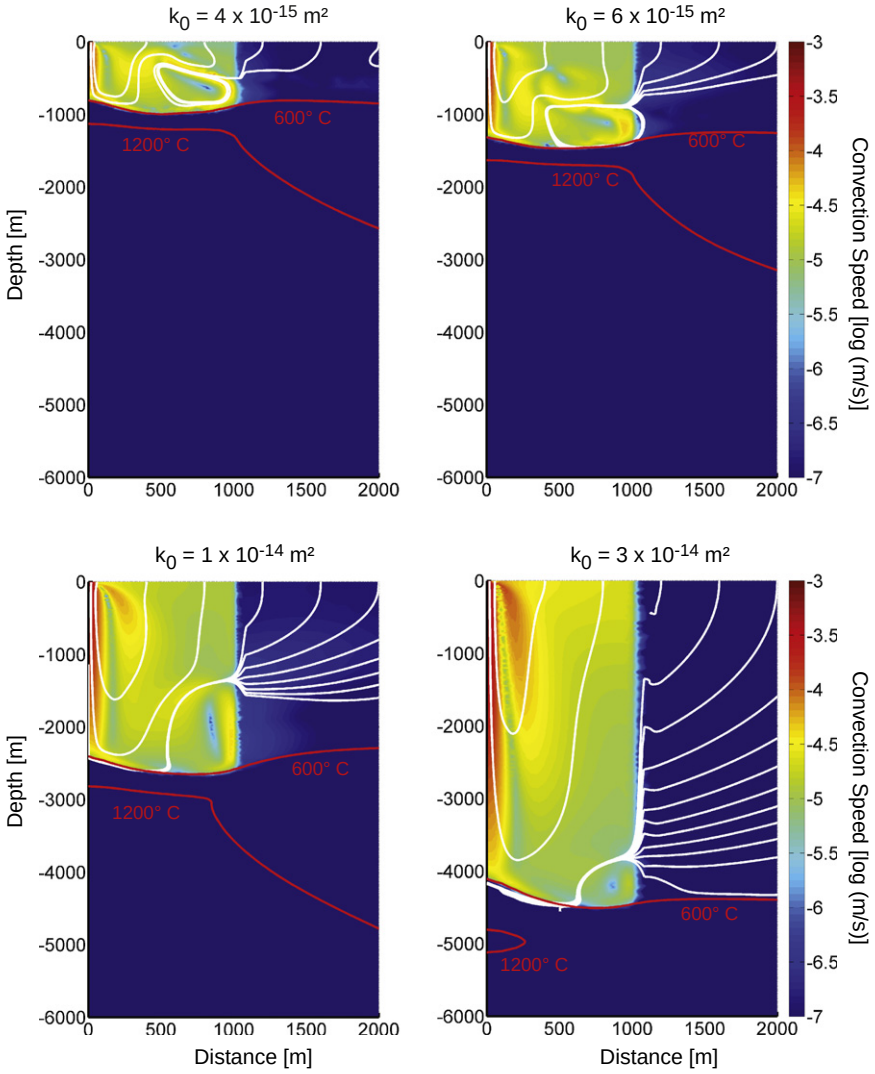

Fig. 6. Convection speed above the melt lens for different surface permeabilities. White streamlines indicate the direction of the fluid flow. The crust is crust is assumed to be impermeable (upper red line) above the cut-off temperature (600 °C). The width of the hot region (1200 °C) is also plotted in the figure (lower red line). The crust is cooled by only one convection cell when surface permeabilities are higher than 6×10^{-15} m^2. (For interpretation of the references to color in this figure legend, the reader is referred to the web version of this article.)

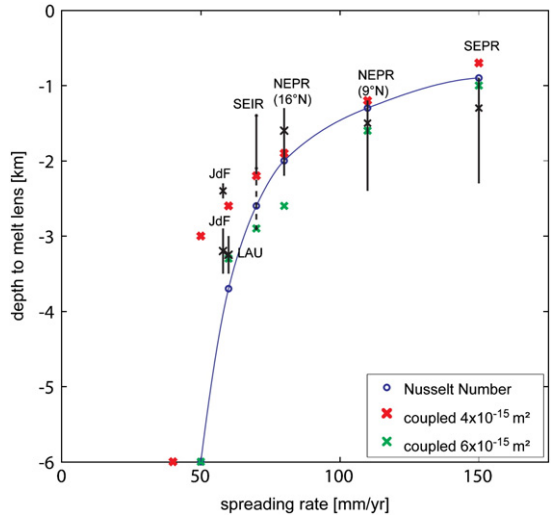

Fig. 7. Depth vs. spreading rate for the coupled model. Blue line shows the results from the parameterized model for comparison. Red crosses are the results for the coupled models with surface permeabilities of 4×10^{-15} m^2; green crosses for a model with a near axis surface permeability of 6×10^{-15} m^2. Labels are the same as in Fig. 3. (For interpretation of the references to color in this figure legend, the reader is referred to the web version of this article.)

crosses) and 6×10^{-15} m^2 (green crosses) is shown in Fig. 7. The calculated depth to the melt lens (1200 °C isotherm at the ridge axis) varies from 700 m for a spreading rate of 150 mm/yr to 3 km for a spreading rate of 50 mm/yr for a near axis surface permeability of 4×10^{-15} m^2. No melt lens is stable below spreading rates of 50 mm/yr. At higher permeabilities (6×10^{-15} m^2) the melt lens stabilizes at 1 km for fast rates (150 mm/yr) and at 3.3 km for intermediate rates (60 mm/yr).

Although poorly constrained, permeability is one of the key variables in the model setup. While difficult to estimate from measured values; it strongly influences the intensity of hydrothermal circulation, determines how much latent heat is removed, and shapes the cooling of the crust. Due to the sensitivity of hydrothermal solutions to permeability, we can use them to estimate the effective pore + fracture permeabilities in the axial region. Estimated permeabilities of the upper 1200 m of the oceanic crust vary between 10^{-13} and 10^{-18} m^2 from in situ measurements in boreholes, and vary over a wider range of values if other methods are considered, e.g. core measurements or indirect methods (Fisher, 1998). Only indirect measurements or model-based inferences are available to estimate permeabilities deeper than 1.2 km. The required permeabilities in our model are lower than those proposed by Cherkaoui et al. (2003) who suggested values of at least 4×10^{-14} m^2 to cool the lower crust at the ridge axis. The threshold permeability of about 2×10^{-15} m^2 to enter the regime of convective cooling is comparable with our results for permeabilities at the ridge axis. Purely hydrothermal models (Coumou et al., 2009) use even higher permeabilities of around 10^{-14}–10^{-13} m^2 for the upper 1000 m of the oceanic crust.

Apart from changing the surface permeability, numerical simulations with different exponents for the decay of permeability within the crust were also conducted (cf. Table 2). In the first series of simulations the permeability decreases exponentially with depth by about two orders of magnitude. In the second set of models the permeability changes only about one order of magnitude through the crust, i.e. the permeabilities at depth are greater ($c=3\times10^{-4}$ m^{-1}). The results are different for fast spreading rates and (slower) intermediate rates. The depth to the melt lens varies only a few tens of meters for fast rates. Slower intermediate spreading rates are much more sensitive to changes in permeability, e.g. for 70 mm/yr the depth to the melt lens is about 1 km deeper compared to models where the permeability decreases by two orders of magnitude.

The cut-off temperature also influences the computed depth to the melt lens significantly. The importance of cracking temperature is different for fast and (slower) intermediate spreading velocities. The difference is largest for slow intermediate spreading rates (80 mm/yr and less) where the melt lens stabilizes around 1 km deeper for 100 °C higher (700 °C) cracking temperature. A cut-off temperature of at least 400 °C is necessary to remove enough heat to stabilize a melt lens in the crust for fast intermediate to fast spreading velocities (110 and 150 mm/yr). Higher cut-off temperatures of hydrothermal circulation will reduce the required permeabilites to match the observed depth to the melt lens. Any predictions of the possible permeability structures are therefore directly related to the chosen temperature of hydrothermal penetration.

5.2.2. Width of the hot region and off-axis temperature

The melt lens overlies a partially molten body in the lower crust, sometimes interpreted as axial magma chamber (Nicolas et al., 2003). In this study the body below the melt lens enclosed by the 1200 °C isotherm (Fig. 8) is defined as a region with high temperatures. We compare the computed half-width of that body with the result of the numerical simulations of Cherkaoui et al. (2003) and the seismic study of Dunn et al. (2000).

The half width of the region with high temperatures at 6 km depth is around 8 km for a spreading rate of 110 mm/yr (EPR). The width decreases with slower spreading velocity and increasing permeability, for 80 mm/yr (comparable to NEPR at 16°N) the half width decreases to 2.7 km. The half-width of the hot lower crust in our model is smaller compared to the models of Cherkaoui et al. (2003) who computed half width of more than 12 km at Moho depth (for permeabilities of 7×10^{-15} m^2), but still larger than Dunn et al. (2000) concluded from a tomographic study at the EPR. They describe a 3.5 km wide partially molten body (half width) at 6 km depth with steep temperature gradients at the ridge axis and flat isotherms away from the melt lens. The off-axis temperature is mainly controlled by the off-axis permeability. A higher surface permeability of 2×10^{-15} m^2 leads to more vigorous convection, deeper hydrothermal cells in the crust and therefore to more efficient cooling from the side (Fig. 8, middle panel). The resulting half-width of the region of hot crust is around 5 km at the Moho and less than 1 km at the top. The high permeabilities off-axis however extract much more heat in the crust and result in temperatures of around 300 °C at the Moho at a distance of 60 km from the axis. The model with lower off-axis permeabilities (1×10^{-16} m^2) stabilizes the temperature at the Moho at around 600–700 °C, similar to the analytical plate cooling solution (cf. Fig. 4). The temperature at the ridge axis and therefore the depth to the melt lens (1.0 km for high off-axis permeability compared to 1.1 km for 10^{-16} m^2) is not influenced by changes in off-axis permeability. In the model setups, permeability only depends on depth while other factors influencing permeability, e.g. thermal cracking related to cooling rate, mineral precipitation that may alter permeability, etc., are not considered. Therefore, a model setup where permeability also decreases with distance to the axis is probably more realistic and will lead to flat isotherms off-axis (as shown for the model with 1×10^{-16} m^2), that steepens towards the ridge axis (as observed with 2×10^{-15} m^2, Fig. 8).

It is possible that three-dimensional hydrothermal effects could further narrow the hot region beneath the melt lens. Intuitively, fluid flow should be more vigours along-axis due to higher along-axis permeability (e.g. parallel to the strike of faults) than across-axis permeability (Coumou et al., 2008). This could lead to deeper near-axis fluid penetration for the same 'average' rock permeability. However, we cannot investigate this potential factor with our current 2D numerical model of hydrothermal circulation.

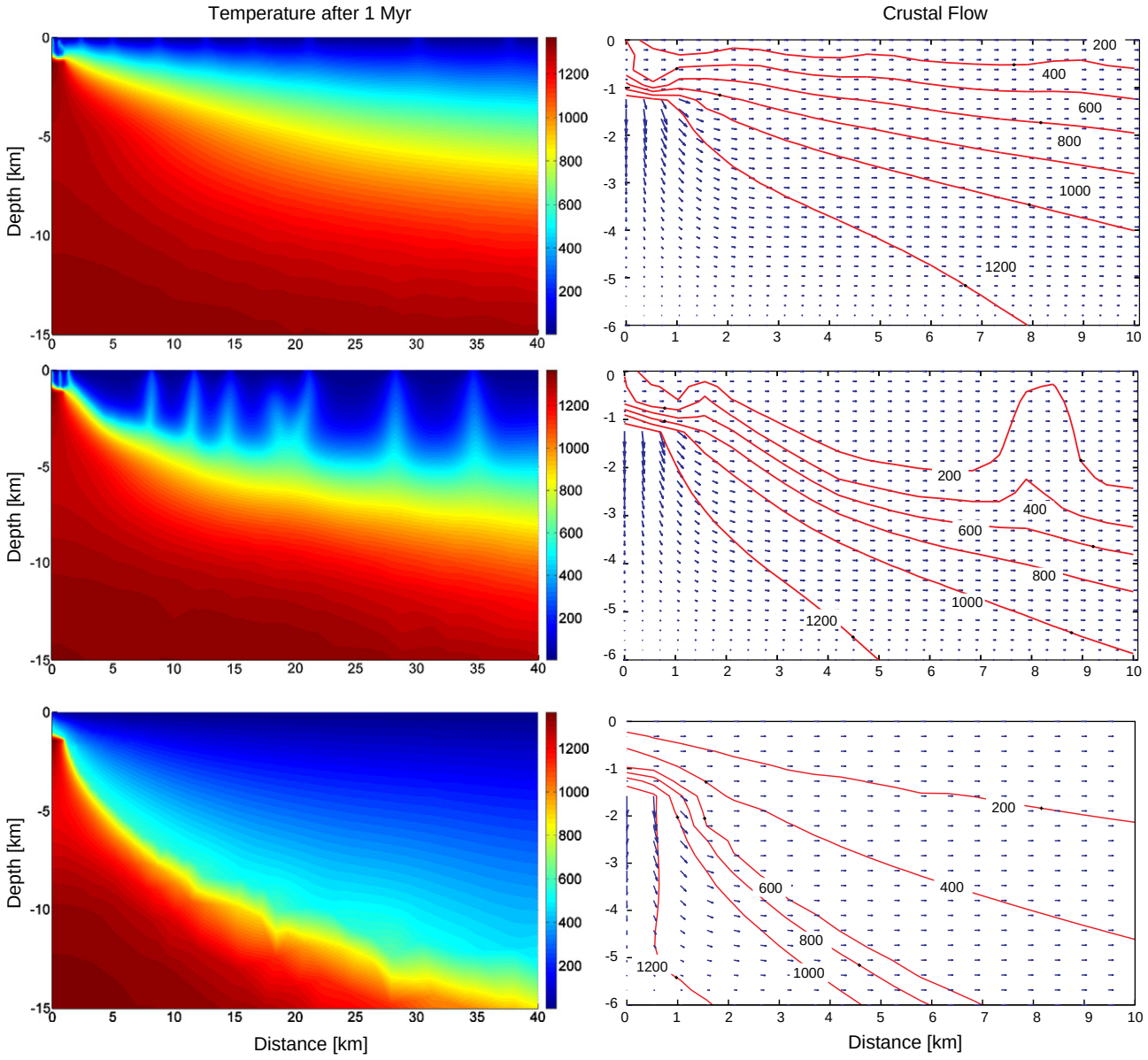

Fig. 8. Influence of off-axis permeability. Left panel shows the temperature structure after 1 Myr modeling time. In the right panel the isotherms and velocity structure for the first 10 km in the crust are plotted. The top row results from a model setup with off-axis surface permeabilities (k^0) of 10^{-16} m^2 and the middle row is the result of higher off-axis surface permeability of 2×10^{-15} m^2. The permeability at the ridge axis is in both model setups the same (4×10^{-15} m^2). Higher off-axis permeability leads to more vigorous convection and a decrease in melt lens half width whereas the depth of the melt lens in both models does not change. The results of the Nusselt number parameterization are shown in the bottom row for comparison. Spreading velocity for all models is 110 mm/yr.

5.3. Depth to the melt lens vs. spreading velocity

The dependency of the depth to the melt lens on spreading velocity is one of the results from modeling crustal accretion and hydrothermal cooling at intermediate to fast spreading ridges. The relation is observed in both the parameterized model that reproduces the results of Phipps Morgan and Chen (1993b) as well as in the coupled crustal + hydrothermal flow model. This depth dependency seems more obvious in the numerical experiments than is shown by measurements. It is also possible to classify the measured data into two groups; at fast to high intermediate spreading rates (Northern EPR, Southern EPR and Southeast Indian Ridge) the observed melt lens is at 1.2–1.8 km depth, whereas at slow intermediate rates (Lau Basin and Juan de Fuca Ridge) a melt lens has been imaged at depth of 2.5–3.5 km. Carbotte et al. (1998) use similar values to classify fast to high intermediate and intermediate to slow spreading rates. Over a total range of 70 mm/yr to 150 mm/yr spreading rate, the melt lens is located around 1.5 km below the seafloor. The melt lens imaged at 2.9 km at Southeast Indian Ridge coincides with thinner crust (Baran et al., 2009). The jump from 1.5 to around 3 km of the melt lens also coincides with a change from axial highs (shallow melt lens) to shallow axial valleys (Baran et al., 2009; Carbotte et al., 1998). Phipps Morgan and Chen (1993a) implemented variable crustal thicknesses in their model and showed that the depth to the melt lens also depends on magma supply. Thicker crust leads to more latent heat release within the melt lens to account for the formation of the entire lower gabbroic section, which stabilizes the melt lens at shallower depths. It was possible to fit the depth to the melt lens at the slow spreading Reykjanes Ridge with such a model setup accounting for crustal thickness. Buck et al. (1997) relate the depth to the melt lens with the thickness of the extrusive layer 2A and found a good agreement for ridges with axial highs. Their model predicts a thicker layer 2A associated with a deeper melt lens.

Our results for higher permeabilities (6×10^{-15} m^2) match the observed depth to the melt lens for high spreading rates (110 and 150 mm/yr) and are consistent with the 50–60 mm/yr transitional spreading rate between median valley and an axial high (no melt lens and melt lens transition), but less consistent with the depth to the melt lens at intermediate rates (60–80 mm/yr). The depth to the melt lens for the intermediate rates can be achieved with lower permeabilities which in turn is less consistent with transitional spreading rate. A melt lens can exist for spreading rates greater than 40 mm/yr. This is consistent with the result of Phipps Morgan and Chen (1993b) where the models with higher cooling (Nu = 12) match the measured melt lens at very high spreading rates. They point out that higher cooling is more consistent up to the spreading rate at which a melt lens becomes stable, which would coincide with the transition between axial high and medial valley morphology (60–70 mm/yr), but less consistent with the measured depth to the melt lens at those "transitional" spreading velocities. These findings suggest that the permeability structure at very fast spreading ridges differs from ridges that spread at intermediate rates. Different crustal permeability models were necessary to match the observed depth to the melt lens and the transition between melt lens and no melt lens for intermediate and fast spreading ridges.

6. Conclusions

A new model of crustal accretion and hydrothermal circulation has been developed. The main difference from previous parameterized models is that we simultaneously resolve crustal generation, crustal deformation, and hydrothermal circulation within one coupled model. Our key results are:

- Coupled 2D simulations are computationally feasible despite the different spatial and temporal scales of crustal accretion and hydrothermal cooling.
- All coupled simulations approach a quasi-steady state for the structure of temperature and deformation. This confirms that a quasi-stable melt lens can exist even though hydrothermal flow may, at the same time, show time dependent variations on shorter time scales. The dependence of melt lens depth on spreading velocity has been confirmed. However, models continue to show a stronger relationship between the two than is observed in available global seismic data sets, perhaps highlighting the additional dependence of lens depth on along-axis and time-dependent variations in crustal supply and crustal thickness.
- Permeability is the key unknown in coupled simulations with model predictions being highly sensitive to it. Small changes in permeability lead to large differences in the predicted temperature structure. Melt lens depths can be fitted with on-axis surface permeabilites of $3–6\times10^{-15}$ m^2. The observed depth vs. spreading-rate dependence of the melt lens may therefore be used to estimate the ridge in-situ permeability structure.
- The depth of hydrothermal convection is affected by the cut-off temperature and permeability. Deep hydrothermal circulation has not been considered to be necessary in the gabbro glacier assumption, but it influences the shape of the hot lower crust significantly and moreover seems to be required to model a narrow hot region as observed in tomographic studies.

Acknowledgments

We would like to thank Harro Schmeling, William Wilcock and all anonymous referees for their helpful reviews. We also thank the editor Yanick Ricard for suggestions to improve the paper.

References

Baker, E.T., 2009. Relationships between hydrothermal activity and axial magma chamber distribution, depth, and melt content. Geochem. Geophys. Geosyst. 10.
Baker, E.T., German, C.R., 2004. On the global distribution of hydrothermal vent fields. In: German, C.R., Lin, J., Parson, L.M. (Eds.), Mid-ocean Ridges: Hydrothermal Interactions between the Lithosphere and Oceans. American Geophysical Union, Washington DC, p. 318.
Baran, J.M., Cochran, J.R., Carbotte, S.M., Nedimovic, M.R., 2005. Variations in upper crustal structure due to variable mantle temperature along the Southeast Indian Ridge. Geochem. Geophys. Geosyst. 6, 21.
Baran, J.M., Cochran, J.R., Holmes, R.C., Tolstoy, M., Carbotte, S.M., 2009. Constraints on the mantle temperature gradient along the Southeast Indian Ridge from crustal structure and isostasy: implications for the transition from an axial high to an axial valley. Geophys. J. Int. 179, 144–153.
Bauer, O., 1998. PROST 4.1 PROperties of Water and STeam, Hamburg.
Bird, R.B., Stewart, W.E., Lightfoot, E.N., 2007. Transport Phenomena, 2nd ed. John Wiley & Sons Inc., New York.
Boudier, F., Nicolas, A., Ildefonse, B., 1996. Magma chambers in the Oman ophiolite: fed from the top and the bottom. Earth Planet. Sci. Lett. 144, 239–250.
Buck, W.R., Carbotte, S.M., Mutter, C., 1997. Controls on extrusion at mid-ocean ridges. Geology 25, 935–938.
Cann, J.R., 1974. Model for oceanic crustal structure developed. Geophys. J. R. Astron. Soc. 39, 169–187.
Carbotte, S., Mutter, C., Mutter, J., Ponce-Correa, G., 1998. Influence of magma supply and spreading rate on crustal magma bodies and emplacement of the extrusive layer: insights from the east Pacific rise at lat16 degrees N. Geology 26, 455–458.
Carbotte, S.M., Detrick, R.S., Harding, A., Canales, J.P., Babcock, J., Kent, G., Van Ark, E., Nedimovic, M., Diebold, J., 2006. Rift topography linked to magmatism at the intermediate spreading Juan de Fuca ridge. Geology 34, 209–212.
Carbotte, S.M., Solomon, A., Ponce-Correa, G., 2000. Evaluation of morphological indicators of magma supply and segmentation from a seismic reflection study of the East Pacific Rise 15 degrees 30 ′-17 degrees N. J. Geophys. Res.-Solid Earth 105, 2737–2759.
Chen, Y., Morgan, W.J., 1990. A nonlinear rheology model for midocean ridge axis topography. J. Geophys. Res.-Solid Earth Planet. 95, 17583–17604.
Chen, Y.J., 2001. Thermal effects of gabbro accretion from a deeper second melt lens at the fast spreading East Pacific Rise. J. Geophys. Res.-Solid Earth 106, 8581–8588.
Cherkaoui, A.S.M., Wilcock, W.S.D., Dunn, R.A., Toomey, D.R., 2003. A numerical model of hydrothermal cooling and crustal accretion at a fast spreading mid-ocean ridge. Geochem. Geophys. Geosyst. 4.
Collier, J., Sinha, M., 1990. Seismic images of a magma chamber beneath the Lau Basin back-arc spreading center. Nature 346, 646–648.
Cordery, M.J., Morgan, J.P., 1992. Melting and mantle flow beneath a mid-ocean spreading center. Earth Planet. Sci. Lett. 111, 493–516.
Corliss, J.B., Dymond, J., Gordon, L.I., Edmond, J.M., Herzen, R.P.V., Ballard, R.D., Green, K., Williams, D., Bainbridge, A., Crane, K., Vanandel, T.H., 1979. Submarine thermal springs on the Galapagos Rift. Science 203, 1073–1083.
Coumou, D., Driesner, T., Geiger, S., Heinrich, C.A., Matthai, S., 2006. The dynamics of mid-ocean ridge hydrothermal systems: splitting plumes and fluctuating vent temperatures. Earth Planet. Sci. Lett. 245, 218–231.
Coumou, D., Driesner, T., Geiger, S., Paluszny, A., Heinrich, C.A., 2009. High-resolution three-dimensional simulations of mid-ocean ridge hydrothermal systems. J. Geophys. Res. 114.
Coumou, D., Driesner, T., Heinrich, C.A., 2008. The structure and dynamics of mid-ocean ridge hydrothermal systems. Science 321, 1825–1828.
Crawford, W.C., Webb, S.C., Hildebrand, J.A., 1999. Constraints on melt in the lower crust and Moho at the East Pacific Rise, 9 degrees 48 ′ N, using seafloor compliance measurements. J. Geophys. Res.-Solid Earth 104, 2923–2939.
Dabrowski, M., Krotkiewski, M., Schmid, D.W., 2008. MILAMIN: MATLAB-based finite element method solver for large problems. Geochem. Geophys. Geosyst. 9.
Detrick, R.S., 2000. Seafloor spreading — portrait of a magma chamber. Nature 406, 578–579.
Detrick, R.S., Buhl, P., Vera, E., Mutter, J., Orcutt, J., Madsen, J., Brocher, T., 1987. Multichannel seismic imaging of a crustal magma chamber along the East Pacific Rise. Nature 326, 35–41.
Dunn, R.A., Toomey, D.R., Solomon, S.C., 2000. Three-dimensional seismic structure and physical properties of the crust and shallow mantle beneath the East Pacific Rise at 9 degrees 30′N. J. Geophys. Res.-Solid Earth 105, 23537–23555.
Faust, C.R., Mercer, J.W., 1979. Geothermal reservoir simulation 1. Mathematical models for liquid- and vapor-dominated hydrothermal systems. Water Resour. Res. 15, 23–30.
Fehn, U., Cathles, L.M., 1979. Hydrothermal convection at slow-spreading mid-ocean ridges. Tectonophysics 55, 239–260.
Fisher, A.T., 1998. Permeability within basaltic oceanic crust. Rev. Geophys. 36, 143–182.
France, L., Ildefonse, B., Koepke, J., 2009. Interactions between magma and hydrothermal system in Oman ophiolite and in IODP Hole 1256D: fossilization of a dynamic melt lens at fast spreading ridges. Geochem. Geophys. Geosyst. 10, 30.
Garg, S.K., Pritchett, J.W., 1977. On pressure-work, viscous dissipation and the energy balance relation for geothermal reservoirs. Adv. Water Resour. 1, 41–47.
Gregory, R.T., Taylor, H.P., 1981. An oxygen isotope profile in a section of Cretaceous oceanic-crust, Samail Ophiolite, Oman — evidence for delta-18-o buffering of the oceans by deep (less-than 5 km) seawater-hydrothermal circulation at mid-ocean ridges. J. Geophys. Res. 86, 2737–2755.
Harding, A.J., Orcutt, J.A., Kappus, M.E., Vera, E.E., Mutter, J.C., Buhl, P., Detrick, R.S., Brocher, T.M., 1989. Structure of young oceanic-crust at 13-degrees-N on the

East Pacific Rise from expanding spread profiles. J. Geophys. Res.-Solid Earth Planet. 94, 12163–12196.
Herron, T.J., Stoffa, P.L., Buhl, P., 1980. Magma chamber and mantle reflections — East Pacific Rise. Geophys. Res. Lett. 7, 989–992.
Hooft, E.E., Detrick, R.S., 1993. The role of density in the accumulation of basaltic melts at mid-ocean ridges. Geophys. Res. Lett. 20, 423–426.
Iyer, K., Rüpke, L.H., Morgan, J.P., 2010. Feedbacks between mantle hydration and hydrothermal convection at ocean spreading centers. Earth Planet. Sci. Lett. 296, 34–44.
Kelemen, P.B., Koga, K., Shimizu, N., 1997. Geochemistry of gabbro sills in the crust–mantle transition zone of the Oman ophiolite: implications for the origin of the oceanic lower crust. Earth Planet. Sci. Lett. 146, 475–488.
Kent, G.M., Singh, S.C., Harding, A.J., Sinha, M.C., Orcutt, J.A., Barton, P.J., White, R.S., Bazin, S., Hobbs, R.W., Tong, C.H., Pye, J.W., 2000. Evidence from three-dimensional seismic reflectivity images for enhanced melt supply beneath mid-ocean-ridge discontinuities. Nature 406, 614–618.
Koepke, J., Feig, S.T., Snow, J., 2005. Hydrous partial melting within the lower oceanic crust. Terra Nova 17, 286–291.
Lowell, R.P., Rona, P.A., Vonherzen, R.P., 1995. Sea-floor hydrothermal systems. J. Geophys. Res.-Solid Earth 100, 327–352.
Lowell, R.P., Seewald, J.S., Metaxas, A., Perfit, M.R., 2008. Modeling seafloor hydrothermal processes: magma to microbe—an overview. In: Lowell, R.P., Seewald, J.S., Metaxas, A., Perfit, M.R. (Eds.), Magma to Microbe: Modeling Hydrothermal Processes at Oceanic Spreading Centers. American Geophysical Union, Washington DC, pp. 1–13.
Machetel, P., Garrido, C.J., 2009. A thermomechanical numerical model for crustal accretion of medium to fast spreading mid-ocean ridges. Geochem. Geophys. Geosyst. 10.
Maclennan, J., Hulme, T., Singh, S.C., 2004. Thermal models of oceanic crustal accretion: linking geophysical, geological and petrological observations. Geochem. Geophys. Geosyst. 5, 32.
Manning, C.E., MacLeod, C.J., Weston, P.E., 2000. Lower-crustal cracking front at fast-spreading ridges: evidence from the East Pacific Rise and the Oman Ophiolite. Geol. Soc. Am. Spec. Pap. 349, 261–272.
McCollom, T.M., Shock, E.L., 1998. Fluid–rock interactions in the lower oceanic crust: thermodynamic models of hydrothermal alteration. J. Geophys. Res.-Solid Earth 103, 547–575.
Morgan, J.P., Chen, Y.J., 1993a. Dependence of ridge-axis morphology on magma supply and spreading rate. Nature 364, 706–708.
Morgan, J.P., Chen, Y.J., 1993b. The genesis of oceanic-crust — magma injection, hydrothermal circulation, and crustal flow. J. Geophys. Res.-Solid Earth 98, 6283–6297.
Morgan, J.P., Harding, A., Orcutt, J., Kent, G., Chen, Y.J., Michael, P.R., 1994. Chapter 7 An Observational and Theoretical Synthesis of Magma Chamber Geometry and Crustal Genesis along a Mid-ocean Ridge Spreading Center, International Geophysics. Academic Press, pp. 139–178.
Morton, J.L., Sleep, N.H., 1985. A mid-ocean ridge thermal-model — constraints on the volume of axial hydrothermal heat-flux. J. Geophys. Res.-Solid Earth Planet. 90, 1345–1353.
Morton, J.L., Sleep, N.H., Normark, W.R., Tompkins, D.H., 1987. Structure of the Southern Juan-de-Fuca Ridge from seismic-reflection records. J. Geophys. Res.-Solid Earth Planet. 92, 11315–11326.
Nehlig, P., Juteau, T., 1988. Flow porosities, permeabilities and preliminary data on fluid inclusions and fossil thermal gradients in the crustal sequence of the Sumail ophiolite (Oman). Tectonophysics 151, 199–221.
Nicolas, A., Mainprice, D., Boudier, F., 2003. High-temperature seawater circulation throughout crust of oceanic ridges: a model derived from the Oman ophiolites. J. Geophys. Res.-Solid Earth 108.
Pallister, J.S., Hopson, C.A., 1981. Samail ophiolite plutonic suite — field relations, phase variation, cryptic variation and layering, and a model of a spreading ridge magma chamber. J. Geophys. Res. 86, 2593–2644.
Purdy, G.M., Kong, L.S.L., Christeson, G.L., Solomon, S.C., 1992. Relationship between spreading rate and the seismic structure of mid-ocean ridges. Nature 355, 815–817.
Quick, J.E., Denlinger, R.P., 1993. Ductile deformation and the origin of layered gabbro in ophiolites. J. Geophys. Res.-Solid Earth 98, 14015–14027.
Ryan, M.P., 1994. Magmatic Systems, International Geophysics. Academic Press Inc.
Schmeling, H., Marquart, G., 2008. Crustal accretion and dynamic feedback on mantle melting of a ridge centred plume: the Iceland case. Elsevier Science Bv, pp. 31–52.
Sclater, J.G., Francheteau, J., 1970. The implications of terrestrial heat flow observations on current tectonic and geochemical models of the crust and upper mantle of the earth. Geophys. J. R. Astron. Soc. 20, 509–542.
Sleep, N.H., 1975. Formation of oceanic crust — some thermal constraints. J. Geophys. Res. 80, 4037–4042.
Stein, C.A., Stein, S., 1992. A model for the global variation in oceanic depth and heat-flow with lithospheric age. Nature 359, 123–129.
Talwani, M., Windisch, C., Langseth Jr., M., 1971. Reykjanes ridge crest: a detailed geophysical study. J. Geophys. Res. 76, 473–517.
Van Ark, E.M., Detrick, R.S., Canales, J.P., Carbotte, S.M., Harding, A.J., Kent, G.M., Nedimovic, M.R., Wilcock, W.S.D., Diebold, J.B., Babcock, J.M., 2007. Seismic structure of the Endeavour Segment, Juan de Fuca Ridge: correlations with seismicity and hydrothermal activity. J. Geophys. Res.-Solid Earth 112.
Violay, M., Pezard, P.A., Ildefonse, B., Belghoul, A., Laverne, C., 2010. Petrophysical properties of the root zone of sheeted dikes in the ocean crust: a case study from Hole ODP/IODP 1256D, Eastern Equatorial Pacific. Tectonophysics 493, 139–152.
Zienkiewicz, O.C., Taylor, R.L., 2000. The Finite Element Method, 5th ed. Butterworth-Heinemann, Oxford, U.K.